PAPER

Check for updates

Morphology-controlled green synthesis of tellurium nanostructures and applications of Te/MXene hybrid structures†

Mengchen Xu,‡[a] Jinshu Li,‡[b] Qingshan Yang,[b] Lu Jiang,[a] Jiaqi He, [ID][c]
Dawei He, [ID] *[a] Yongsheng Wang*[a] and Yajie Yang [ID] *[a]

Tellurium (Te), a striking elemental nanomaterial, demonstrated anisotropic physical properties owing to its unique chiral-chain van der Waals structure. Here, morphology-controlled Te nanostructures are synthesized by a viable and eco-friendly solution process, realizing the formation of high-quality two-dimensional (2D) tellurene and one-dimensional (1D) Te nanostructures with controlled morphologies, including nanotubes, nanowires, and nanocables. A reasonable growth mechanism was derived to explain the morphology transformation. Moreover, the two-dimensional material MXene ($Ti_3C_2T_x$) was introduced to fabricate transparent conductive electrodes based on Te/MXene hybrid structures, in which low sheet resistance (156 Ω sq^{-1}) and high transmittance (70%) were obtained.

Introduction

Recently, Te nanostructures have attracted considerable attention due to their unique van der Waals structure and intriguing physical and chemical properties, which are fundamentally different from those of layered van der Waals materials.[1–8] High-quality Te nanostructures could be synthesized by solution processes in which intriguing shape transformation occurs in the presence of a surfactant. First, the formation of cylindrical seeds (0D) was observed experimentally, facilitating the subsequent growth along the $\langle 001 \rangle$ direction of these seeds until the formation of a 1D nanostructure. As the reaction continues, the 1D Te nanostructure will transform into 2D tellurene with the assistance of a surfactant.[9–12] Studies about the growth mechanism and morphology control are necessary for the further commercial development of Te nanomaterials.[13] However, in the current aqueous processes of synthesizing Te nanostructures, the most productive reductant is hydrazine hydrate, which is toxic, lethal, and destructive to the earth, which seriously limits the applications of Te nanostructures.[14–16]

In this paper, a viable and eco-friendly solution process is performed to prepare Te nanomaterials by using biomolecule glucose as the green reductant. Conveniently, glucose can be used as both a reductant and a surfactant at the same time,[17] which could avoid the addition of an extra surfactant and improve the quality of the obtained Te nanostructures. By simply modulating the reaction temperature, we can obtain Te 1D nanostructures with various morphologies, including nanotubes, nanowires, and nanocables. Moreover, 2D tellurene was observed with a prolonged reaction time. Scanning electron microscopy (SEM), X-ray powder diffraction (XRD), X-ray photoelectron spectroscopy (XPS), Raman spectroscopy, and transition electron microscopy (TEM) measurements were utilized to confirm the morphologies of the synthesized Te nanostructures.

Te nanostructures exhibited outstanding performance in different fields, including electronics, optoelectronics, and energy storage.[18–23] Thereinto, Te nanowire networks are excellent candidates to fabricate indium tin oxide (ITO)-free, flexible transparent conductive electrodes (TCEs), regarding their optical transparency, electrical conductance, and mechanical performance.[24–27] However, the shortfall of a pure nanowire TCE is evident when considering its intrinsic limitations, such as the existence of large voids of insulation at a microscopic level, which limits their micro-level conductivity. MXene ($M_{n+1}X_nT_x$), a new class of 2D transition-metal carbides and carbonitrides, has been attracting ongoing attention due to their high metallic conductivity, hydrophilicity, and stability.[28–32] The involvement of MXene is supposed to be an effective way to make up the insulated voids and improve the stability and surface roughness of the TCE as a cover layer of Te networks.[33] Here, a Te/MXene hybrid structure was prepared

[a] Key Laboratory of Luminescence and Optical Information, Ministry of Education, Institute of Optoelectronic Technology, Beijing Jiaotong University, Beijing 100044, China. E-mail: dwhe@bjtu.edu.cn, yshwang@bjtu.edu.cn, yangyj@bjtu.edu.cn

[b] SKKU Advanced Institute of Nanotechnology (SAINT), Sungkyunkwan University, Suwon 16419, South Korea

[c] College of Mathematics and Physics, Beijing University of Chemical Technology, Beijing 100029, China

† Electronic supplementary information (ESI) available. See DOI: https://doi.org/10.1039/d3ma00579h

‡ These authors contributed equally to this work.

through lay-by-layer spray coating. Compared with pure Te networks, this hybrid structure shows a significant decrease in sheet resistance and an unobvious increase in transmittance. Finally, high transparency (70%) and high conductivity (156 Ω sq^{-1}) were achieved for this hybrid structure, making it an excellent candidate for application as a transparent conductive electrode.

Results and discussion

Fig. 1 shows the SEM and TEM images of the synthesized 1D Te nanostructures at different reaction temperatures. The detailed synthesis process is explained in the Experimental section, and the schematic diagram of the synthesis process is shown in Fig. S1 (ESI†), in which the biomolecule glucose, instead of toxic hydrazine hydrate, is used as the reductant and sodium tellurite (Na_2TeO_3) is used as the Te source. As shown in Fig. 1, various morphologies and dimensions were obtained at different growth temperatures. At 90 °C, a shuttle-like tubular structure of tellurium with 80 nm diameter and 1.7 μm length was formed (Fig. 1(a)), illustrating a similar morphology to that of the reported tellurium nanotubes.[10] The inset in Fig. 1(a) shows a magnified view of the tubular structure. At 120 °C, the shape of the synthesized Te crystals transformed to nanowires with a diameter of 25 nm (Fig. 1(b)), and the inserted TEM image confirms the smooth surface and accurate dimensions of Te nanowires (Te NWs). Similar results were observed at 150 °C

in Fig. 1(c), where Te nanowires with relatively decreased dimensions (ca. 23 nm) showed up. When the temperature is increased to 180 °C, as shown in Fig. 1(d), the synthesized products exhibit an obvious core–shell structure, which is identified by the inserted TEM image with obvious contrast between the outer shell (ca. 30 nm) and the inner core (ca. 25 nm), indicating the structure of nanocables.[12,34]

To further identify the characteristics of the prepared 1D Te nanostructures, a series of measurements were performed. XPS is employed to investigate the components and chemical bonding. Fig. S2 (ESI†) and Fig. 2(a), (b) show the XPS survey spectra of Te nanotubes, Te NWs, and Te nanocables. The Te 3d peaks of the Te nanotubes and nanowires exhibit apparently high intensity. In contrast, for Te nanocables, the peaks of carbon and oxygen show relatively high intensity, indicating that Te NWs are buried within the carbonaceous sheets and confirmed the Te/C nanocable structures.[12,35] The high-resolution XPS spectrum of the C 1s peak is shown in Fig. S3 (ESI†), in which the peaks at 286.1 and 287.9 eV are attributed to the residue groups of C–OH and C=O.[12] Because of the small detecting depth of XPS, the Te 3d peak with a binding energy of ∼573 eV for Te nanocables is nearly undetectable in Fig. 2(b) due to the existence of a carbon shell. The detailed Te 3d XPS spectrum is shown in Fig. 2(c), in which two peaks at 573 and 583 eV are assigned to the Te(0) 3d binding energy, and two relatively weak peaks at 576 eV and 586 eV can be attributed to the Te(ıv) 3d binding energy. These Te 3d peaks suggest the successful synthesis of element Te in the
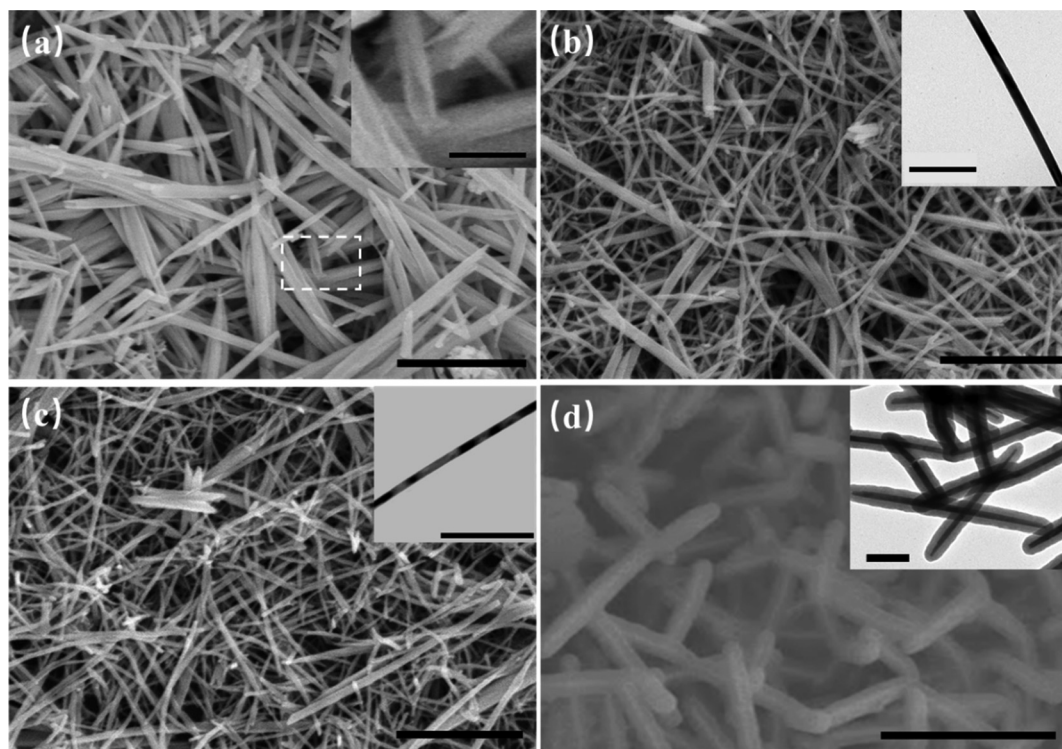

Fig. 1 SEM images of the tellurium nanostructures prepared at different reaction temperatures. (a) At 90 °C, tellurium nanotubes were obtained. The inset is the high magnification of the shuttle-like scrolled nanotubes of tellurium. (b) and (c) At 120 °C and 150 °C, tellurium nanowires were obtained. The inset is the TEM image of tellurium nanowires. (d) At 180 °C, core/shell nanocables were synthesized. The inset is the TEM image of tellurium nanocables. Scale bar: 1 μm in the main figures and 200 nm in the insets.
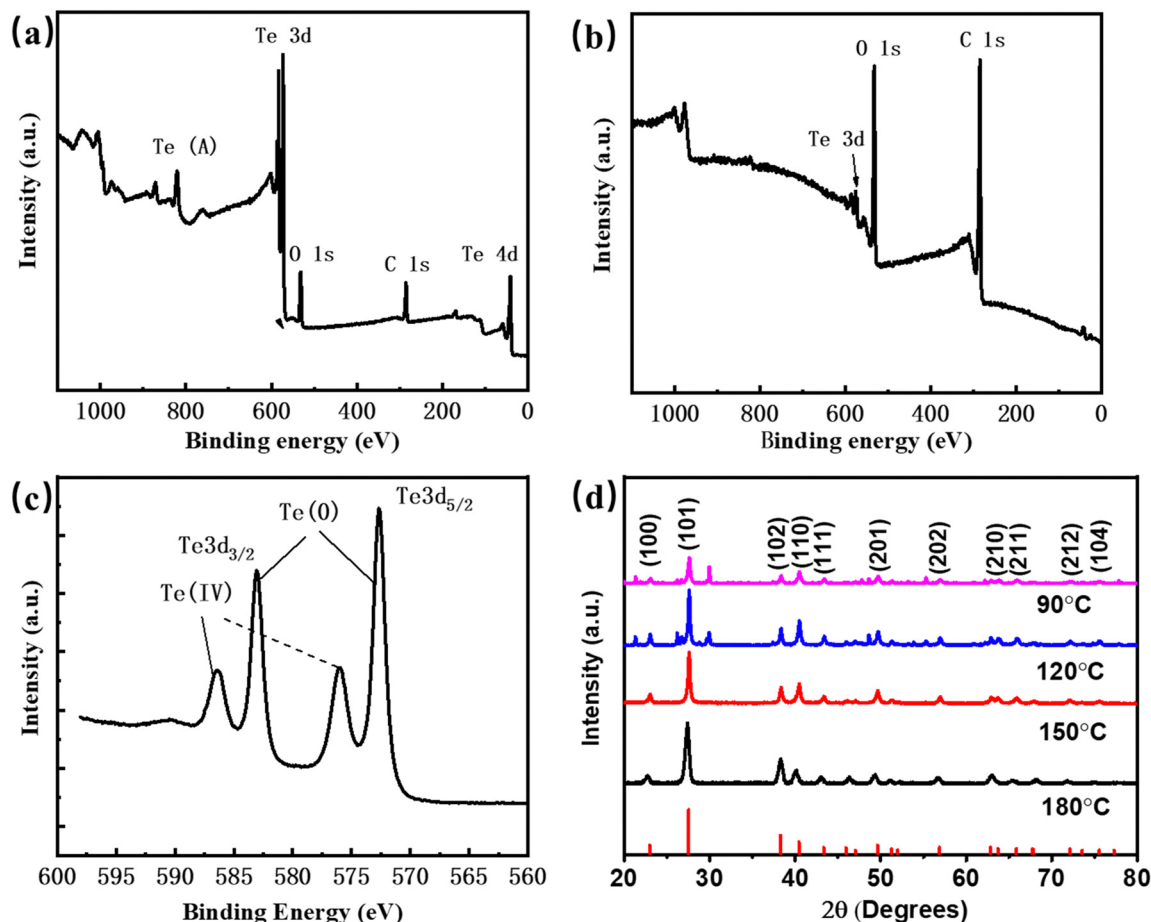
Fig. 2 (a) and (b) Wide-range XPS spectra of the products prepared at 120 °C and 180 °C, respectively. (c) High-resolution XPS spectra of Te 3d. (d) XRD patterns of the synthesized Te nanomaterials at different reaction temperatures.

presence of glucose reductant. XRD measurement was employed to further analyze the purity and crystallinity of these Te nanostructures. The spectra are shown in Fig. 2(d). All the diffraction peaks of these patterns can be indexed according to the trigonal structure of Te, in which the spiral chains of Te atoms are aligned parallel to each other along the longitudinal axis of each Te nanostructure.[20,34,36,37] The calculated lattice constants are $a = 4.4471$ and $c = 5.9117$, which are consistent with the reported values of $a = 4.468$ and $c = 5.927$ (JPCDS card, no. 36-1452).

The schematic diagram in Fig. 3 demonstrates the morphology-controlled synthesis process of Te 1D nanostructures. The reduction reaction can be expressed in the following equation:[38]
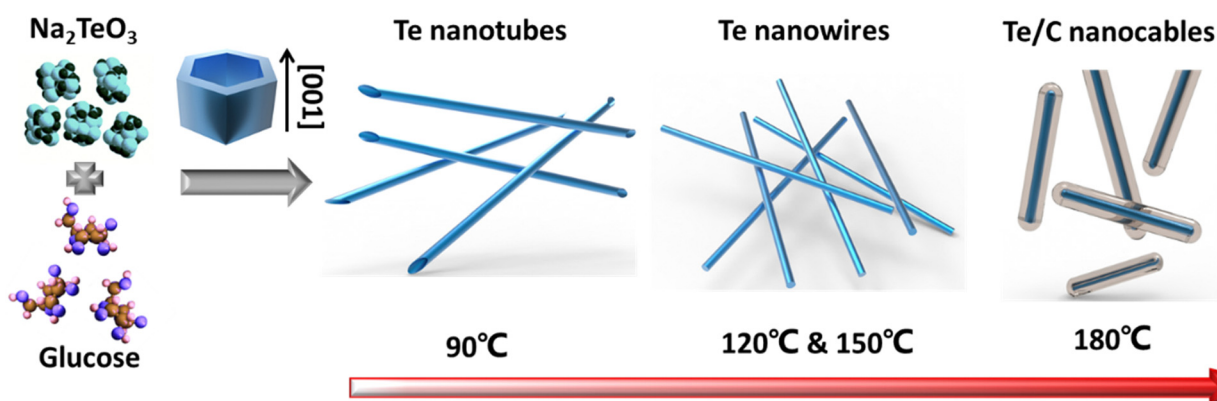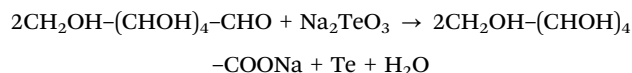
$$2CH_2OH-(CHOH)_4-CHO + Na_2TeO_3 \rightarrow 2CH_2OH-(CHOH)_4-COONa + Te + H_2O$$

Fig. 3 Schematic illustration of the morphology-controlled synthesis of Te 1D nanostructures.

© 2023 The Author(s). Published by the Royal Society of Chemistry

The reaction temperature is a critical factor in this reduction reaction for achieving the wide morphologies of tellurium. Increasing the reaction temperature results in a greater frequency and a force of collisions of the reactant particles, which means that the reactants are more likely to surmount the activation energy barrier and form Te atoms. At 90 °C, the reduction reaction processed relatively slowly, and the resultant Te atoms would preferentially occur at the circumferential edges of each cylindrical seed due to their higher free engines than other sites on the surfaces,[39,40] leading to the deficiency of tellurium atoms for the growth of the central portions of the growing faces, {001} planes, of each seed. Therefore, the tubular structures were synthesized because there was no mass transport to the inner regions. The synthesized Te nanotubes show distinct ends like sleeve-fish tails, which are supposed to be formed by the scrolling mechanism.[10] Bamboo leaf-like nanostructures were formed on the surfaces of Te seeds first. With time prolonging, hypogenetic scrolls of tellurium were formed and became longer and curled, forming the smooth shuttle-like nanotubes with two ends open. As the temperature increased to 120 °C, enough tellurium atoms could be provided by the reduction reaction. Thus, Te NWs would be formed instead of the tubular structure. As the reaction temperature increased to 180 °C, the temperature was higher than the normal glycosidation temperature of glucose, leading to aromatization and carbonization. The carbonization of glucose led to the formation of an amorphous carbon layer on the surface of Te NWs, forming Te/C nanocables.

Besides 1D nanostructures, 2D tellurene can also be synthesized by this green solution process, in which shape transformation from 1D to 2D will take place with an extended reaction time in the presence of surfactants.[11] By employing glucose as the reductant and surfactant, we prolonged the reaction time from 24 to 40 hours and kept other parameters unchanged. Subsequently, 2D tellurene could be examined using the Raman spectra, OM, and SEM images, as shown in Fig. S4 (ESI†). The lateral dimension of the synthesized tellurene was ~10 μm, and the crystal structure of tellurene was identified by its three typical vibration modes located at 92, 121, and 141 cm^{-1}.[5,11]

We explored the electrical properties of the synthesized Te nanostructures. Benefitting from the dual function of glucose as both the reductant and surfactant, the obtained Te nanostructures show enhanced electrical properties by eliminating the impurities induced by the addition of an extra surfactant. As demonstrated in Fig. S5 (ESI†), Te NWs show high conductivity and low transconductance (poor gate controllability), indicating the potential for transparent conductive electrode applications. Te networks were spray-coated on the SiO$_2$ substrate in high uniformity, as shown by the SEM image in Fig. 4(a). To make up the insulated voids of Te networks at
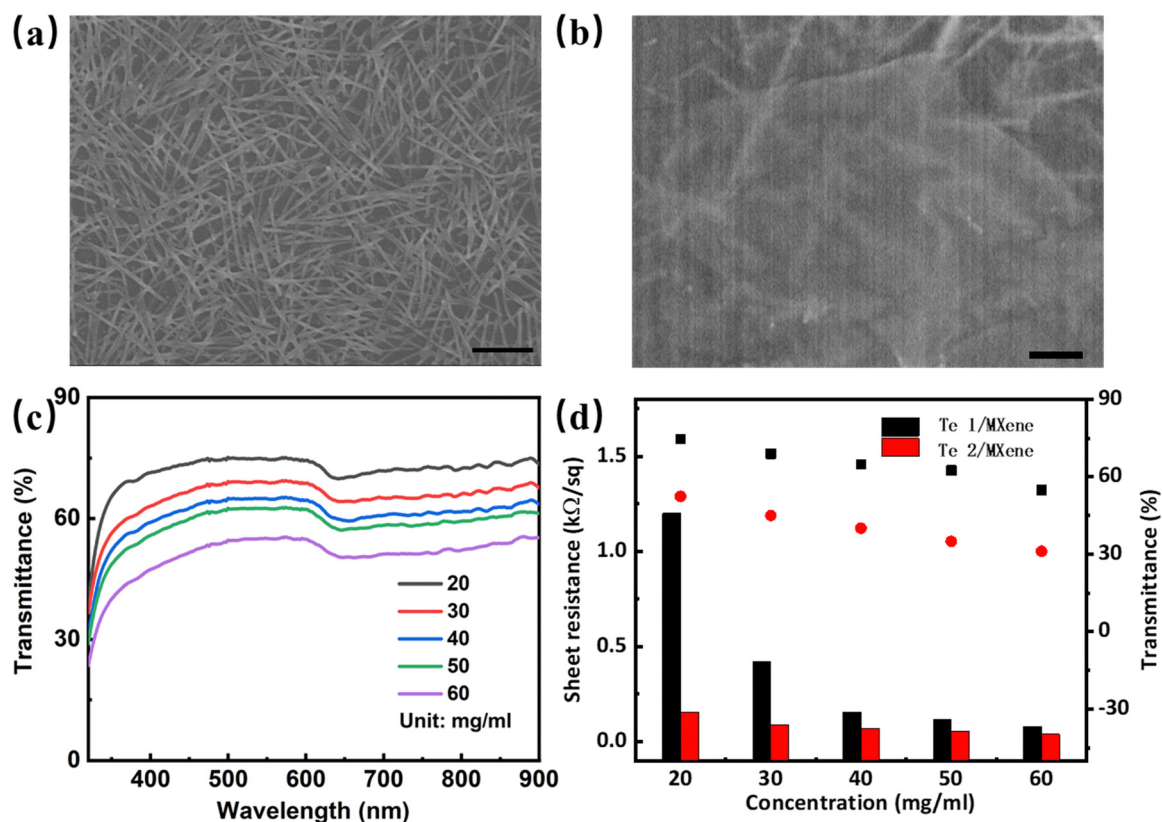

Fig. 4 (a) and (b) SEM images of Te NW films and Te NW/MXene hybrid structures. Scale bar, 0.5 μm. (c) Transmission spectra of Te NWs/MXene hybrid structures with different solution concentrations of Te NWs. (d) Sheet resistances and transmittances of Te NWs/MXene hybrid structures with different solution concentrations of Te NWs. Te 1/MXene: Te/MXene hybrid structures with one layer of Te NWs. Te 2/MXene: Te/MXene hybrid structures with two layers of Te NWs.

the microscopic scale, highly conductive two-dimensional MXene ($Ti_3C_2T_x$) flakes were induced. $Ti_3C_2T_x$ nanoflakes were exfoliated by the typical liquid exfoliation process (details are in the Experimental section), and their XRD patterns, OM, and SEM images are shown in Fig. S6 (ESI†). The solution of the obtained $Ti_3C_2T_x$ nanosheets (20 mg mL^{-1}) was coated on the prepared Te NW networks, forming Te NWs/$Ti_3C_2T_x$ hybrid structures, as demonstrated in Fig. S7 (ESI†). Fig. 4(b) shows the SEM images of the top view of Te NWs/$Ti_3C_2T_x$ hybrid structures, in which Te networks are covered by $Ti_3C_2T_x$ flakes. The UV-vis-NIR spectrum is utilized to investigate the optical characteristics of Te NWs/$Ti_3C_2T_x$ hybrid films with different solution concentrations of Te NWs (Fig. 4(c)). A broad absorption peak at around 700 nm and an absorption peak in the UV region were verified as the typical characteristics of MXene films.[41] The sheet resistances of Te NWs/$Ti_3C_2T_x$ TCEs were evaluated using a sheet resistance meter. The transmittances at 550 nm wavelength and sheet resistances of Te and Te/MXene TCEs with different Te NW concentrations are shown in Fig. S8 (ESI†). With the spray-coating of the MXene layer, Te/MXene demonstrates significant performance enhancement with obvious lower sheet resistances and similar transmittances. Fig. 4(d) summarizes the transmittances and sheet resistances of Te NWs/$Ti_3C_2T_x$ with different Te NW concentrations. The engagement of the $Ti_3C_2T_x$ cover layer results in negligible increases of transmittances but significant reductions of sheet resistances. Finally, a low sheet resistance of 420 Ω sq^{-1} and a high transmittance of 70% were achieved. The solution concentration of MXene was also modulated to analyze the optoelectrical properties of Te/MXene TCEs (Fig. S9, ESI†), and a sheet resistance of 156 Ω sq^{-1} and a high transmittance of 70% were achieved. A comparison of various transparent conductive electrodes based on nanomaterials is shown in Table S1 (ESI†), in which the Te/MXene TCE shows an obvious advantage.

Conclusions

In summary, the morphology-selected synthesis of low-dimensional tellurium nanostructures is realized using a green solution process. The morphologies of the synthesized nanomaterials are determined by two process parameters: the reaction temperature and time. With the process temperature increasing from 90 °C to 180 °C, Te nanotubes, nanowires, and Te/C nanocables can be obtained, respectively. The biomolecule glucose is employed as the reductant and surfactant in the synthesis process, which avoids the addition of an extra surfactant and results in a high quality of the prepared nanomaterials. Then, a $Ti_3C_2T_x$ cover layer was introduced to make up the insulated voids of a pure Te NW film and improve its stability in the air. Finally, a high-performance transparent electrode with a low sheet resistance (156 Ω sq^{-1}) and a high transmittance (70%) was realized with a Te/MXene hybrid structure.

Experimental section

Synthesis of Te nanostructures

To synthesize tellurium 1D nanostructures, sodium tellurite (Na_2TeO_3, ≥99%) was used as the tellurium source. Glucose

was added as the reductant and surfactant. First, 2.9904 g of glucose (Analytical Reagent, AR) and 0.105 g of Na_2TeO_3 were mixed and dissolved in 60 mL of deionized (DI) water under stirring to form a homogeneous solution. The mixed solution was poured into a 100 mL Teflon-lined stainless-steel autoclave. The autoclave was sealed and kept at certain reaction temperatures for 12 hours. The obtained mixture was washed with DI water 3 times (centrifugation, 5000 rpm × 5 min per cycle). For the synthesis of 2D tellurene, the reaction temperature was fixed at 120 °C and the reaction was extended to 40 hours.

Synthesis of MXene ($Ti_3C_2T_x$) nanosheets

1 g of Ti_3AlC_2 power was slowly added to a premixed etchant solution containing a lithium fluoride (LiF) salt (1.6 g) and hydrochloric acid (12 M, 30 mL). The obtained mixture was allowed to stand for 24 h at 40 °C and then washed with deionized water. With consecutive centrifugation (3500 rpm × 3 min per cycle) until the pH of the supernatant is ~6, delamination is completed.

Characterization

Scanning electron microscopy (S-4800, Hitachi) and transmission electron microscopy (JEM-1400, JEOL) measurements were performed to measure the morphologies of the synthesized Te nanostructured materials. X-ray photoelectron spectroscopy (Thermo Scientific, Thermo Fisher) was performed to understand the chemical composition of the synthesized Te nanostructure. The phase structure was characterized by X-ray diffraction (Bruker D8 advance). Raman spectra were recorded using a laser micro-Raman spectrometer (LabRAM HR Evolution, HORIBA lobin Yvon) with an excitation of a 532 nm laser. The electrical properties were measured using a Keithley 4200 parameter analyzer. Transmittances and sheet resistances were confirmed using a spectroscope (MAX 2000 pro) and a sheet resistance meter (RTS-9).

Author contributions

M. Xu and L. Jiang: experiments; J. Li, J. He, and Q. Yang: analysis, writing the draft, and review. D. He, Y. Wang, and Y. Yang: conceptualization, supervision, and editing.

Conflicts of interest

There are no conflicts to declare.

Acknowledgements

References

1 H. Hu, Y. Zeng, S. Gao, R. Wang, J. Zhao, K. You, Y. Song, Q. Xiao, R. Cao, J. Li, Z. Lin, J. Guo, Y. Shu, Z. Guo and D. Fan, *J. Mater. Chem. C*, 2021, **9**, 508–516.

2 Y. Meng, X. Li, X. Kang, W. Li, W. Wang, Z. Lai, W. Wang, Q. Quan, X. Bu, S. Yip, P. Xie, D. Chen, D. Li, F. Wang, C.-F. Yeung, C. Lan, C. Liu, L. Shen, Y. Lu, F. Chen, C.-Y. Wong and J. C. Ho, *Nat. Commun.*, 2023, **14**, 2431.

3 Y.-H. Chan, C.-Y. Lin, Y.-C. Chou, A. C. Chang, Y.-F. Lin and Y.-Z. Chen, *Mater. Adv.*, 2023, **4**, 2008–2016.

4 G. Qiu, C. Niu, Y. Wang, M. Si, Z. Zhang, W. Wu and P. D. Ye, *Nat. Nanotechnol.*, 2020, **15**, 585–591.

5 J. Lu, Y. He, C. Ma, Q. Ye, H. Yi, Z. Zheng, J. Yao and G. Yang, *Adv. Mater.*, 2023, **35**, 2211562.

6 Y. Zhang, F. Zhang, Y. Xu, W. Huang, L. Wu, Z. Dong, Y. Zhang, B. Dong, X. Zhang and H. Zhang, *Small Methods*, 2019, **3**, 1900349.

7 Y. Zhang, Y. Xu, C. Zhang, J. Guo, Z. Shi, L. Wu, F. Zhang, C. Ma, R. Cao, L. Gao, Y. Ge, X. Zhang and H. Zhang, *J. Mater. Chem. C*, 2020, **8**, 5991–6000.

8 Y. Zhang, F. Zhang, L. Wu, Y. Zhang, W. Huang, Y. Tang, L. Hu, P. Huang, X. Zhang and H. Zhang, *Small*, 2019, **15**, 1903233.

9 B. Mayers and Y. Xia, *Adv. Mater.*, 2002, **14**, 279–282.

10 Z. He, S.-H. Yu and J. Zhu, *Chem. Mater.*, 2005, **17**, 2785–2788.

11 Y. Wang, G. Qiu, R. Wang, S. Huang, Q. Wang, Y. Liu, Y. Du, W. A. Goddard, M. J. Kim, X. Xu, P. D. Ye and W. Wu, *Nat. Electron.*, 2018, **1**, 228–236.

12 W. Wang, L. Sun, Z. Fang, L. Chen and Z. Zhang, *Cryst. Growth Des.*, 2009, **9**, 2117–2123.

13 Z. Li, S. Zheng, Y. Zhang, R. Teng, T. Huang, C. Chen and G. Lu, *J. Mater. Chem. A*, 2013, **1**, 15046–15052.

14 G. Wang, Y. Guan, Y. Wang, Y. Ding and L. Yang, *Materials*, 2023, **16**, 738.

15 V. Adepu, M. Tathacharya, R. Cs, V. Mattela and P. Sahatiya, *ACS Appl. Nano Mater.*, 2022, **5**, 18209–18219.

16 J. Yoon, B. You, Y. Kim, J. Bak, M. Yang, J. Park, M. G. Hahm and M. Lee, *ACS Appl. Mater. Interfaces*, 2023, **15**, 18463–18472.

17 Y. Liu, Q. Jiang, J. Zhang, W. Ding, J. Xu, P. Liu, G. Nie, H. Mao and F. Jiang, *Mater. Adv.*, 2020, **1**, 1125–1133.

18 R. Zheng, K. Zheng and H. Fu, *Appl. Surf. Sci.*, 2011, **257**, 8024–8027.

19 L. Jin, Y. Hao, A. K. Tareen, K. Khan, S. Wageh, O. A. Al-Hartomy, A. G. Al-Sehemi, H. Zhang and Y. Zhang, *J. Mater. Chem. A*, 2023, **11**, 3771–3788.

20 X. Wang, Y. Xu, H. Zhu, R. Liu, H. Wang and Q. Li, *CrystEngComm*, 2011, **13**, 2955.

21 C. Shen, Y. Liu, J. Wu, C. Xu, D. Cui, Z. Li, Q. Liu, Y. Li, Y. Wang, X. Cao, H. Kumazoe, F. Shimojo, A. Krishnamoorthy,

R. K. Kalia, A. Nakano, P. D. Vashishta, M. R. Amer, A. N. Abbas, H. Wang, W. Wu and C. Zhou, *ACS Nano*, 2019, **14**, 303–310.

22 C. Liu, R. Wang and Y. Zhang, *Nanomaterials*, 2022, **12**, 2151.

23 Y. Zhang, J. Guo, Y. Xu, W. Huang, C. Li, L. Gao, L. Wu, Z. Shi, C. Ma, Y. Ge, X. Zhang and H. Zhang, *Nanoscale Horiz.*, 2020, **5**, 847–856.

24 D. Choi, D. Kim, Y. Jo, J. H. Kim, E. Yoon, H.-C. Lee and T. Kim, *Appl. Surf. Sci.*, 2021, **565**, 150521.

25 X. Wei, S. Wang, N. Zhang, Y. Li, Y. Tang, H. Jing, J. Lu, Z. Xu and H. Xu, *Adv. Funct. Mater.*, 2023, **33**, 2300141.

26 M. Xu, J. Xu, L. Luo, M. Wu, B. Tang, L. Li, Q. Lu, W. Li, H. Ying, L. Zheng, H. Wu, Q. Li, H. Jiang, J. Di, W. Zhao, Z. Zhang, Y. He, X. Zheng, X. Gan, Z. Liu, X. Wang and W. Huang, *Mater. Today*, 2023, **63**, 50–58.

27 Y. Ahn, D. Lee, Y. Jeong, H. Lee and Y. Lee, *J. Mater. Chem. C*, 2017, **5**, 2425–2431.

28 H. Ding, Y. Li, M. Li, K. Chen, K. Liang, G. Chen, J. Lu, J. Palisaitis, P. O. Persson and P. J. S. Eklund, *Science*, 2023, **379**, 1130–1135.

29 K. R. G. Lim, M. Shekhirev, B. C. Wyatt, B. Anasori, Y. Gogotsi and Z. W. Seh, *Nat. Synth.*, 2022, **1**, 601–614.

30 A. VahidMohammadi, J. Rosen and Y. Gogotsi, *Science*, 2021, **372**, 1165.

31 Y. Liu, X. Zhang, W. Zhang, X. Ge, Y. Wang, X. Zou, X. Zhou and W. Zheng, *Energy Environ. Mater.*, 2022, e12438.

32 J. Li, W. Zhang, X. Ge, M. Lu, X. Xue, Z. Wang, N. Yue, J. Zhang, X. Lang, Q. Jiang and W. Zheng, *J. Energy Chem.*, 2022, **72**, 26–32.

33 E.-Y. Shin, S. B. Choi, J. H. Lee, B. Yoo, C. J. Han, S. H. Park, J. H. Noh, J.-W. Kim and H. J. Son, *Sol. RRL*, 2023, **7**, 2201130.

34 G. S. Cao, C. W. Dong, L. Wang and Z. S. Liu, *Mater. Lett.*, 2009, **63**, 1778–1780.

35 G. Xi, C. Wang, X. Wang, Y. Qian and H. Xiao, *J. Phys. Chem. C*, 2008, **112**, 965–971.

36 G. S. Cao, Y., G. Liu, W. W. Yang, C. Tan, H. Li and X. J. Zhang, *Bull. Mater. Sci.*, 2011, **34**, 1185–1188.

37 J. Chen, Y. Gao, J. Yang, Q. Wang, Y. Cao, K. Jiang, Y. Li, J. Zhang, L. Zhu, L. Shang, Z. Hu and J. Chu, *IEEE Electron Device Lett.*, 2022, **43**, 1776–1779.

38 Q. Chen, G. Liu, G. Chen, T. Mi and J. J. B. Tai, *BioResources*, 2017, **12**, 608–621.

39 Z. Liu, S. Li, Y. Yang, Z. Hu, S. Peng, J. Liang and Y. Qian, *New J. Chem.*, 2003, **27**, 1748.

40 G. Krueger and C. J. T. J. o C. P. Miller, *J. Chem. Phys.*, 1953, **21**, 2018–2023.

41 P. Salles, D. Pinto, K. Hantanasirisakul, K. Maleski, C. E. Shuck and Y. Gogotsi, *Adv. Funct. Mater.*, 2019, **29**, 1809223.